Journal of Solid State Electrochemistry (2022) 26:1585–1603
https://doi.org/10.1007/s10008-022-05193-z

ORIGINAL PAPER

Salt spray corrosion behavior and pitting resistance of Ti-15 V-3Cr-3Al-3Sn alloy evaluated using XPS, SKPFM, and electrochemical technique

Longfei Xie[1] · **Wenlong Zhou**[1,2]

Received: 26 January 2022 / Revised: 10 April 2022 / Accepted: 19 May 2022 / Published online: 28 May 2022

Abstract

As a promising material for many industrial applications, Ti-15 V-3Cr-3Al-3Sn (commonly referred to as Ti-15–3) titanium alloy always suffers from non-uniform pitting corrosion in salt spray environment. Herein, based on electrochemical impedance spectroscopy (EIS), electrochemical noise (EN) tests, and surface analysis, we systematically evaluate the salt spray corrosion behaviors of Ti-15–3 alloy by a 3.5 wt.% NaCl solution test. EN analysis based on Hilbert-Huang transform investigates corrosion types of Ti-15–3 alloy corroded by salt spray, combining with further electrode/solution interface behavior and corrosion resistance analysis from EIS. This combined investigation demonstrated that metastable pitting, passive state, and the stable pitting of Ti-15–3 alloy for a different salt spray time were successfully distinguished. Meanwhile, it was found that pitting resistance and corrosion types were closely connected with the corrosion attack morphology of the corroded samples, together with an investigation of the micrographs of the damaged surface. Finally, the salt spray corrosion mechanisms of Ti-15–3 alloy are discussed in detail. This work will provide significant insights into the service life and protection measures of tropical ocean facilities to avoid the attack of pitting corrosion.

Keywords Electrochemical impedance spectroscopy · Electrochemical noise · Pitting corrosion · Electrochemical reactions · Hilbert-Huang transform

Introduction

Ti-15 V-3Cr-3Al-3Sn (commonly referred to as Ti-15–3) alloy is considerable material in aerospace and automotive fields due to its excellent cold deformability, high strength-to-weight ratio, and good corrosion resistance [1]. However, the space launch facility is built near the tropical ocean area, encountering serious corrosion of some natural environmental factors, such as seawater, salt spray, and humidity. Among these factors, chloride is always thought to be the most crucial one in the degeneration of marine structures, because it gathers on the surface of Ti-15–3 alloy used in aerospace launch tower parts and aggravates its corrosion [2, 3]. To be precise, the attack of chlorides can cause some small pits on the surface of titanium alloy, and these pits further bring about the breakage and the failure of the equipment [4, 5]. Hence, it is crucial to evaluate the corrosion behavior of Ti-15–3 alloy in a salt spray environment.

Many studies in the literature have shown that the pitting corrosion and passivation behavior of titanium alloy is frequently observed in chloride media. Kolman and Scully [6] studied the effect of composition and concentration of the solution on the passivity characterization of titanium alloy Ti-15–3 in chloride-containing solutions and concluded that beta titanium alloy possesses spontaneous passivity behavior. Sun et al. [7] found that the destruction of the passive film appears when titanium alloy TC4 is exposed to salt spray for a long time. However, it is difficult to explore and monitor the rupture and renovation of titanium alloy using conventional electrochemical techniques (such as open circuit potential, OCP, and/or polarization curves). Although electrochemical

---

✉ Wenlong Zhou
wlzhou@126.com

[1] Key Laboratory of Solidification Control and Digital Preparation Technology (Liaoning Province), School of Materials Science and Engineering, Dalian University of Technology, No.2 Linggong Road, Ganjingzi District, Dalian 116024, Liaoning Province, China

[2] Dalian Technology (Yingkou) Advanced Material Engineering Center Company Limited, Yingkou 115004, China

Table 1 Chemical composition (wt.%) of Ti-15–3 alloy

V	Cr	Sn	Al	Fe	Si	C	N	H	O	Ti
13.49	4.18	3.23	5.76	0.07	0.18	0.05	0.05	0.02	0.13	Balance

impedance spectroscopy (EIS), as a nondestructive and reliable electrochemical technique, has been used to investigate the electrode/solution interface and corrosion resistance broadly [8], EIS cannot be used to identify forms of corrosion in passive materials in aggressive media. Recently, electrochemical noise (EN) has been widely used to detect metastable pitting, the rupture, and repair of a surface film as well as stable pitting [9–12].

A powerful approach, the Hilbert-Huang transform (HHT), was applied [13]. The Hilbert spectral analysis is a method of time–frequency analysis of EN signals, which segregates the particular transient signals from the background. This theory comes from the EN data itself directly [14, 15], which is not limited by filter windows of the Fourier transformation [16]. Hoseinieh et al. [17] used Hilbert spectra to research localized corrosion of AISI 316L and mild steel in a 3 wt.% NaCl solution. They found that more local attacks can be differentiated by the small-time constants visible in the high-frequency region of Hilbert spectra. Herein, invisible transients in the time domain were primely identified by obtaining the Hilbert spectrum of a short duration from the electrochemical potential noise (EPN) data. Thereby, it is highly desired to combine electrochemical noise analysis based on Hilbert-Huang transform as well as electrochemical impedance spectroscopy (EIS) to study the pitting corrosion behavior of Ti-15–3 alloy in salt spray environment. From the literature review, it is understood that most of the published researches on titanium alloys were focused on immersion corrosion in biomaterials. Very few investigations have been done to explore the effect of salt spray time on the pitting corrosion behavior of Ti-15–3 alloy. No investigation was carried out by incorporating the relationship between corrosion morphology and corrosion form. Hence, the aim of the present work is to study the effect of salt spray time on the corrosion form of Ti-15–3 alloy. Furthermore, the main contribution of this work is the introduction of a complementary methodology to infer the corrosion types of polished Ti-15–3 alloy after different salt spray time by combining supporting insights from surface characteristics after salt spray, EIS, and Hilbert spectrum analyses acquired in 3.5 wt% NaCl solution.

In this work, microstructure characteristics of the polished Ti-15–3 alloy corroded by salt spray were preliminarily investigated through a scanning electron microscope (SEM) with energy dispersive spectrometer (EDS), confocal laser scanning microscope (CLSM), scanning Kelvin probe force microscopy (SKPFM), and X-ray photoelectron spectroscopy (XPS) analyses. Afterwards, metastable pitting, passive state, and the growth of stable pitting of the polished Ti-15–3 alloy for different salt spray time were successfully distinguished by electrochemical techniques. In addition, combining with the SEM micrographs of the damaged surface, it is found that pitting resistance and surface state are closely connected with the corrosion attack morphology of the corroded samples, and the salt spray corrosion mechanisms of the polished Ti-15–3 alloy is thoroughly discussed.

Experimental

Materials and specimen preparation

The material used in this work was a 2-mm cold-rolled Ti-15 V-3Cr-3Al-3Sn (commonly referred to as Ti-15–3) alloy plate after solution treatment, and the chemical composition of Ti-15–3 alloy was listed in Table 1. Metallographic analysis revealed that the as-received Ti-15–3 alloy involved only α-free β grains, as shown in Fig. 1. The dimension of samples for the NSS test is 25 mm × 25 mm × 2 mm. The sample surfaces were first ground with SiC papers to 2500 grit and then polished with the 0.06-μm silicon oxide suspension. Sample before the neutral salt spray test was soaked in an ultrasonic bath with acetone for 35 min, followed by rinsing with deionized water, and then cleaned with alcohol, finally dried with cold air.

Neutral salt spray test

According to the ASTM B117, the neutral salt spray (NSS) test was carried out with the YQW-250-type test chamber (the main conditions included temperature 35 °C, 5 wt% NaCl solution at pH = 7.0, and ≤ 85% RH ambient humidity).

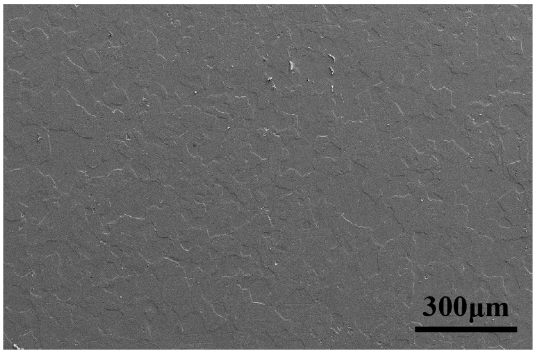

Fig. 1 SEM micrograph shows entirely β phase in the as-received Ti-15–3 alloy sample

The samples were exposed to neutral salt spray for 6 h, 24 h, 72 h, 312 h, and 720 h, respectively. After each salt spray test time, some samples were removed out, and tested immediately in a 3.5 wt.% NaCl to obtain reliable electrochemical data. For each salt spray time, the corroded samples employed in the electrochemical noise (EN) and EIS measurements are different. But, other samples were removed out and rinsed with deionized water to remove redundant salts. Then, these samples were dried and placed in a desiccator for 0.5 h at a temperature of 35 °C to ensure that no further surface reactions occurred. These corroded samples were used for subsequent microstructure characterization.

Microstructural characterization

Surface morphology and element distribution of the samples after the neutral salt spray (NSS) test were examined by SUPRA55-type scanning electron microscope (SEM) with an energy dispersive spectrometer (EDS, Oxford AZtecX-Max80). The chemical composition of the passive film formed on the Ti-15–3 alloy surface was studied using an X-ray photoelectron spectroscopy (XPS, Thermo Scientific ESCALAB 250Xi, America). In addition, the surface topography and Volta potential of deposit and pit were measured by confocal laser scanning microscope (CLSM, OLYMPUS OLS4000, Japan) and scanning Kelvin probe force microscope (SKPFM, Shimadzu instruments, Inc., Japan). The scan rate was set as 0.5 Hz. Because the actual Volta potential is the inversion of measured potential difference obtained by SKPFM, all potential profiles presented are the invert of measured potential [18].

Electrochemical measurements

To further elucidate the effects of different salt spray time on the corrosion properties of Ti-15–3 alloy, the electrochemical measurements were performed at room temperature to study the electrochemical impedance spectroscopy (EIS) and electrochemical noise in a 3.5 wt% NaCl solution. The EIS test used a three-electrode system, with a saturated calomel electrode (SCE) as a reference electrode, a platinum net as an auxiliary electrode, and Ti-15–3 alloy sample (a surface area of 1 cm^2) corroded by salt spray as a working electrode. Prior to the EIS measurements, the sample corroded by salt spray was immersed in the 3.5 wt.% NaCl solution for 1 h to reach a steady-state open circuit potential (OCP). Then, the EIS was measured in the frequency domain of 100 kHz to 5 mHz with an amplitude of 10 mV. Ten points per decade were recorded during EIS measurements. The EIS data were fitted and analyzed using own software of a CS310H-type Autolab electrochemical testing system. For each salt spray time, at least three samples were prepared for electrochemical measurement to ensure the reliability of the experiment.

The electrochemical noise test was carried out with a ZRA system of electrochemical workstation and conducted in the three-electrode cell (Fig. 2) open to the air under stagnant conditions, with a saturated calomel electrode (SCE) as reference electrode, two nominally identical samples corroded by salt spray (exposed to the same salt spray time) as working and counter electrodes, respectively. The measurement was performed at constant room temperature (25 °C). The ground mode is a virtual ground. After 1 h of static immersion in a 3.5 wt% NaCl solution, the sampling frequency is 5 Hz, the EN signals were recorded for 1 h with a data sampling interval of 0.2 s. All the EN tests were repeated three times. The electrochemical potential noise (EPN) signal was analyzed by Hilbert spectral time–frequency. Hilbert spectrum involves the empirical decomposition mode (EMD) and the Hilbert-Huang transform (HHT), which were acquired by own programs (EMD and HHT procedures) of a public MATLAB R2020b. As Homborg et al. have earlier proposed the Hilbert-Huang transform, a detailed step of the application of the Hilbert spectrum for the analysis of EN signals has been introduced [19].

Results

Ti-15–3 alloy native oxide film composition by XPS

The composition of Ti-15–3 alloy native oxide film is evaluated by high-resolution X-ray photoelectron spectra of Ti

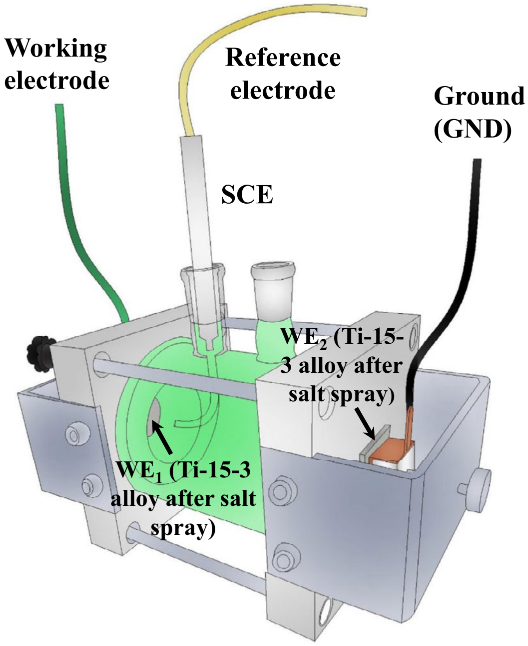

Fig. 2 Electrochemical cell set-up used for EN measurements in ZRA mode

2p, V 2p, Cr 2p, Al2p, Sn 3d, and O 1 s features (Fig. 3). The high-resolution spectrum for Ti 2p (Fig. 3a) indicates the existence of TiO_2 protective oxide and metallic Ti on the Ti-15–3 alloy surface. For Sn 3d, the only oxide formed is the very protective SnO_2 and metallic Sn on the Ti-15–3 alloy surface (Fig. 3b). V 2p is present as protective V_2O_5 oxide (Fig. 3c). Cr 2p is only present as protective Cr_2O_3 oxide (Fig. 3d). Al 2p is only present as protective Al_2O_3 oxide (Fig. 3e). The high-resolution spectrum of O 1 s is well deconvoluted into two peaks (Fig. 3f), corresponding to the formation of the protective TiO_2, V_2O_5, and Cr_2O_3 oxides at 529.8 eV, characteristic for oxides in very high percent (53.5%), the formation of the protective SnO_2 and Al_2O_3 oxides at 531.5 eV, characteristic for oxides in very high percent (46.5%). Undoubtedly, this film contains besides the protective TiO_2 oxide, furthermore, the very protective V_2O_5, Cr_2O_3, SnO_2, and Al_2O_3 oxides, it turns out that this film is highly protective.

Surface morphology of Ti-15–3 alloy

Before salt spray corrosion, the SEM micrograph of the Ti-15–3 alloy surface is smooth without micro-pits, as shown in Fig. 4a. After 24 h of salt spray, some pitting corrosions appear on the Ti-15–3 alloy surface (Fig. 4b). There was little change in the amount of pitting for 312 h of salt spray (Fig. 4c). Figure 4d shows that the amount of pitting corrosions and corrosion products obviously increases at 720 h

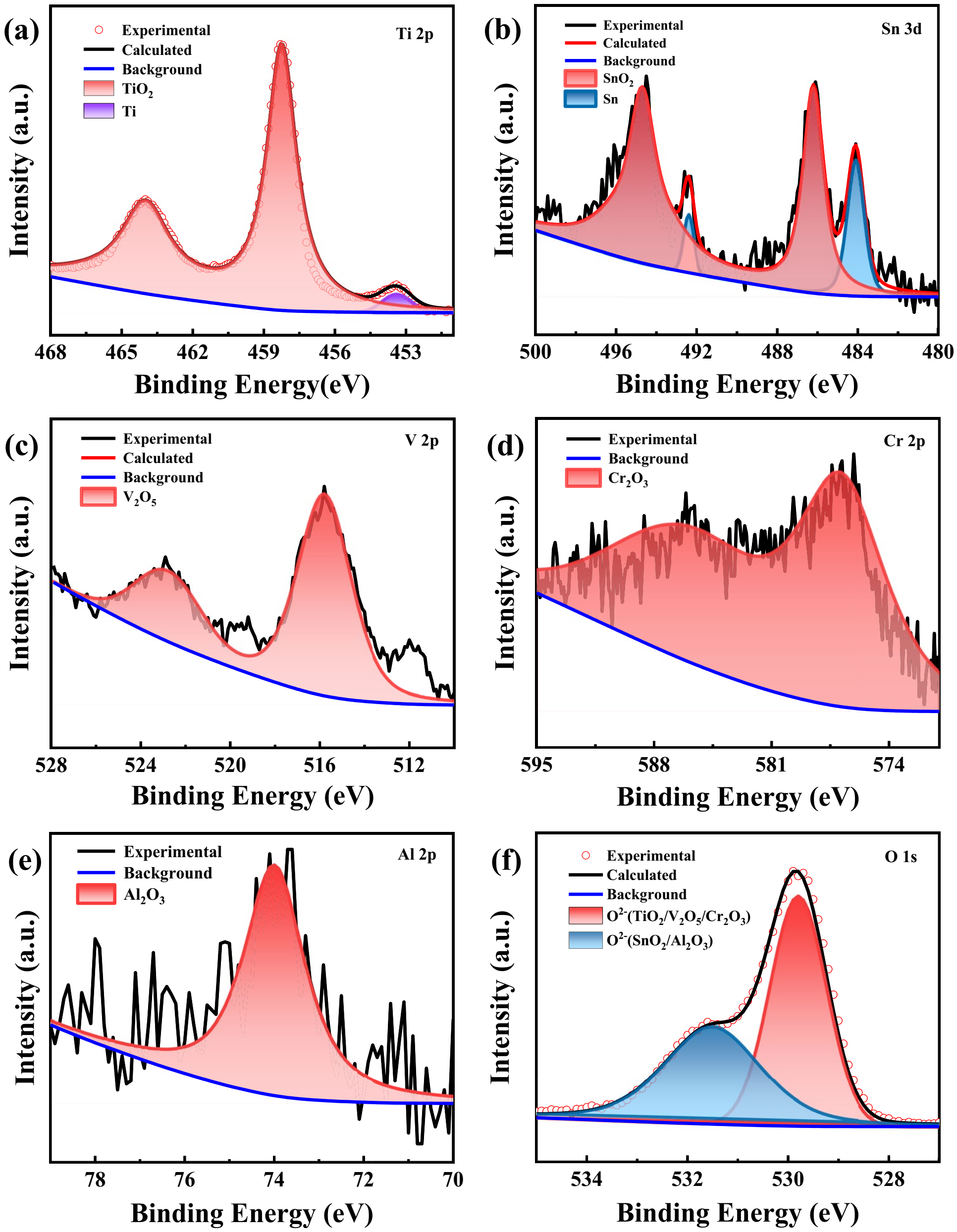

Fig. 3 High-resolution XPS spectra for **a** Ti 2p; **b** Sn 3d; **c** V 2p; **d** Cr 2p; **e** Al 2p; **f** O 1 s obtained of the native oxide film on Ti-15–3 alloy surface

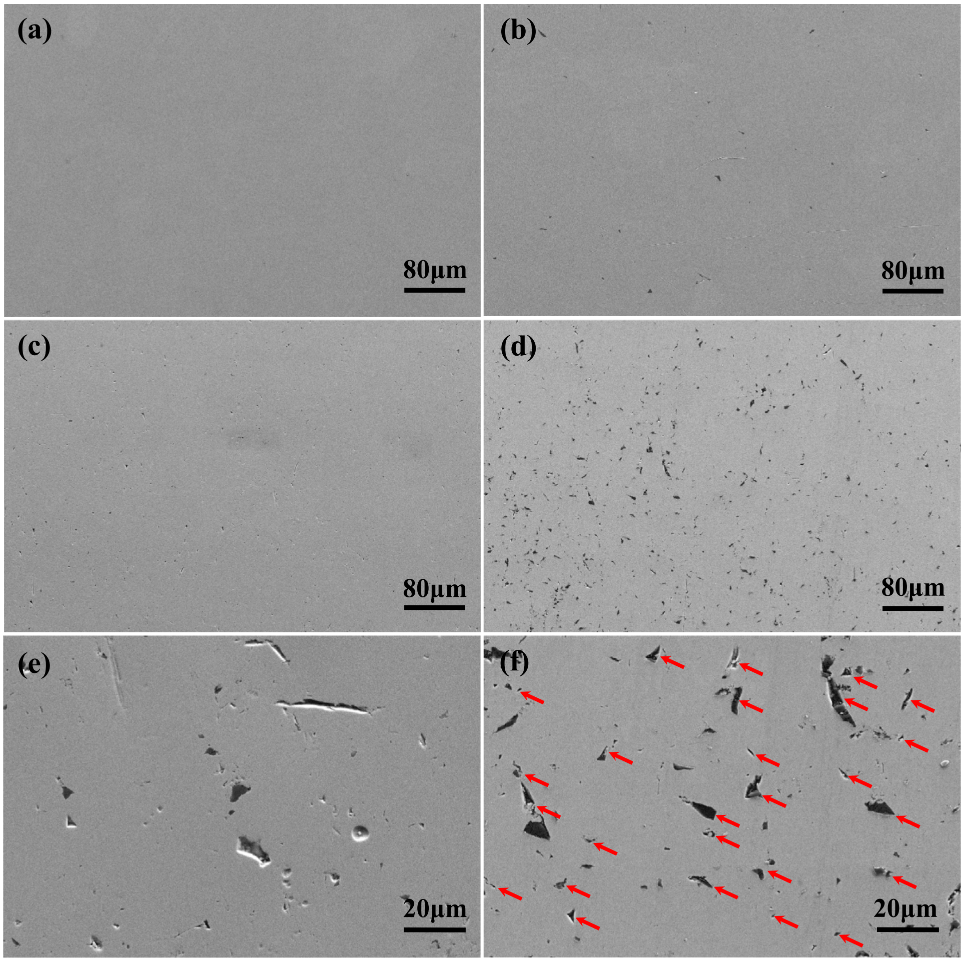

Fig. 4 Low-magnification observation from SEM images of Ti-15–3 alloy samples unexposed to salt spray (**a**); after **b** 24 h, **c** 312 h, and **d** 720 h of NSS test; high-magnification observation from SEM images of Ti-15–3 alloy samples after **e** 312 h and **f** 720 h of the NSS test

of the salt spray test. Compare with Fig. 4e and f shows the existence of the lots of pitting corrosions on a massive area. As can be seen from Fig. 5a, some pitting corrosions (an irregular pit without dark gray deposits), ditches, and dark gray deposits are observed on the Ti-15–3 alloy surface at 6 h of the NSS test. Figure 5b shows that Ti-15–3 alloy surface contains deposit and ditch at 24 h of the salt spray test. The determination of the deposit will be confirmed in the latter "EDS analysis" section. Figure 5c and d show that the Ti-15–3 alloy surface includes some deposits, ditches, and pitting corrosions at 312 h and 720 h of the salt spray test. Obviously, the change of the pit widths on Ti-15–3 alloy surface with time is not apparent when salt spray time increases from 6 to 312 h, the widths of all pitting corrosions and ditches remain about 2 mm (Fig. 5a–c), while the width of pitting corrosion on Ti-15–3 alloy surface for 720 h of the NSS test obviously increases to 5 mm (Fig. 5d). Moreover, the deepest pits determined from CLSM 3D images are shown in Fig. 6. As depicted in Fig. 6, the deepest pits of Ti-15–3 alloy surface for 6 h, 312 h, and 720 h of salt spray are 0.31 μm, 0.22 μm, and 1.24 μm, respectively. Obviously, for 720 h of salt spray, the pit depth on the Ti-15–3 alloy surface is the maximum. As can be seen from Fig. 6a, the deposit measurement of the Ti-15–3 alloy surface at 6 h of salt spray shows that the height of the deposit is higher than that of the metal matrix.

Characterization of corrosion products after salt spray

EDS analysis

In order to study the deposit characteristic of Ti-15–3 alloy surface after the salt spray test, the elemental distribution analyses and corresponding SEM image are shown in Fig. 7; it can be found that six constituent elements of Al, O, Ti, V, Sn, Al, and Cr are distinguished. Meanwhile, on the basis of the color maps for elements distribution, it can be seen from Fig. 7 that the deposit is mainly composed of Al oxide (Al_2O_3).

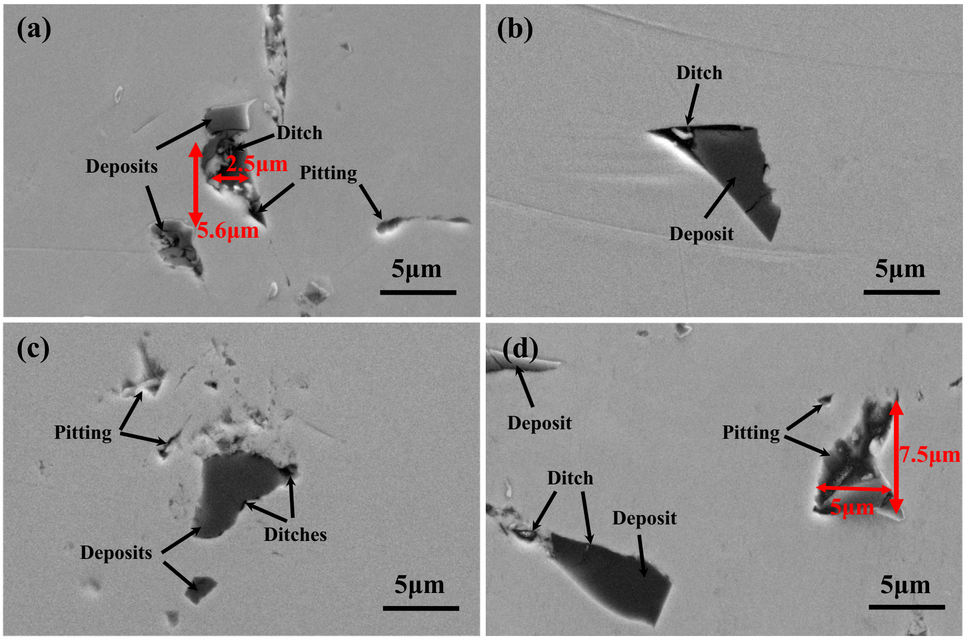

Fig. 5 High-magnification observation from SEM images of Ti-15–3 alloy samples after **a** 6 h, **b** 24 h, **c** 312 h, and **d** 720 h of the NSS test

SKPFM measurement

To acquire particular information about the difference of morphology and localized electrochemical heterogeneity between the deposits (Al oxide) and metal matrix, SKPFM measurement was successively carried out. Meanwhile, in order to facilitate the analysis, the selected region is divided into two parts labeled A-B and C-D (Fig. 8a), the corresponding potential profile is shown in Fig. 8b. Combining with the analysis results of Fig. 8c and d, obviously, the A-B region is ascribed to pitting corrosion with a depth of 0.05 µm (Fig. 8e) and the C-D area corresponds to bulge (blue area) with a height of 0.04 µm and ditch (red area) with a depth of 0.02 µm (Fig. 8f). Likewise, according to Volta potential linear profile (Fig. 8e), the value of Volta potential for the pitting region possesses more negative potential than that of alloy matrix with an intact native oxide film, implying that intact oxide film around the pitting corrosion on Ti-15–3 alloy surface acts as the cathode and its corrosion will be inhibited, while pitting regions acts as anode and its corrosion will be accelerated. Figure 8f shows that the Volta potential of bulge is higher than that of the metal matrix with an intact native oxide film.

According to EDS and CLSM 3D image analyses, it is apparent that the bulges (blue area) with more positive potential are deposits (Al_2O_3). In general, a deposit rich in Al_2O_3 acts as the cathode and its corrosion will be inhibited while the area at its interface with the adjacent matrix acts as an anode and pitting corrosion will be facilitated in the form of a galvanic couple. But, these traditional conclusions are overturned by Liu et al. [20]. They noted that deposits rich in Al_2O_3 could not play a role of cathode due to its high electric resistivity. Therefore, they believed that the high deformation may be considered the main cause of preferential dissolution of metal matrix around deposits (Al_2O_3). Figure 8f confirms that the Volta potential of ditch regions is smaller than that of the metal matrix with an intact native oxide film and deposits (Al_2O_3), implying that intact oxide film around the ditches could play a role in the cathode, while ditch regions act as anode and its corrosion will be promoted. All potential plots presented were the invert of measured potential.

XPS analysis

XPS is used to assess the composition and chemical bonding state on the surface of Ti-15–3 alloy after different salt spray time. The XPS survey spectra of Ti-15–3 alloy surface for 6 h, 312 h, and 720 h of the NSS test are presented in Fig. 9a. The characteristic photoelectron spectroscopy mainly contains Ti 2p, V 2p, Cr 2p, Sn 3d, Al 2p, O 1 s, Na 1 s, Cl 2p, and C 1 s peaks. Ti and O are the dominant elements of titanium oxide. The Na 1 s and Cl 2p come from the residue of salt spray. Figure 9b shows the high-resolution spectra of Ti 2p; the highest peaks of Ti 2p for Ti-15–3 alloy samples after 6 h, 312 h, and 720 h of salt spray are well deconvoluted into a doublet, corresponding to TiO_2 at ~ 458.5 eV, Ti_2O_3 at ~ 457.8 eV. Their another peak can be fitted as a peak, corresponding toTiO_2 at ~ 464.3 eV. In addition, metallic Ti of Ti-15–3 alloy samples, which occurs at ~ 453.4 eV (Ti 2p3/2). As shown in Fig. 9c, the high-resolution spectra of O 1 s for 6 h of salt spray can be fitted to two different components: O^{2-} (530 eV), Me-OH(Ti–OH/Al–OH)/Ti_2O_3 (531.3 eV) [21, 22]; these asymmetric curves are composed

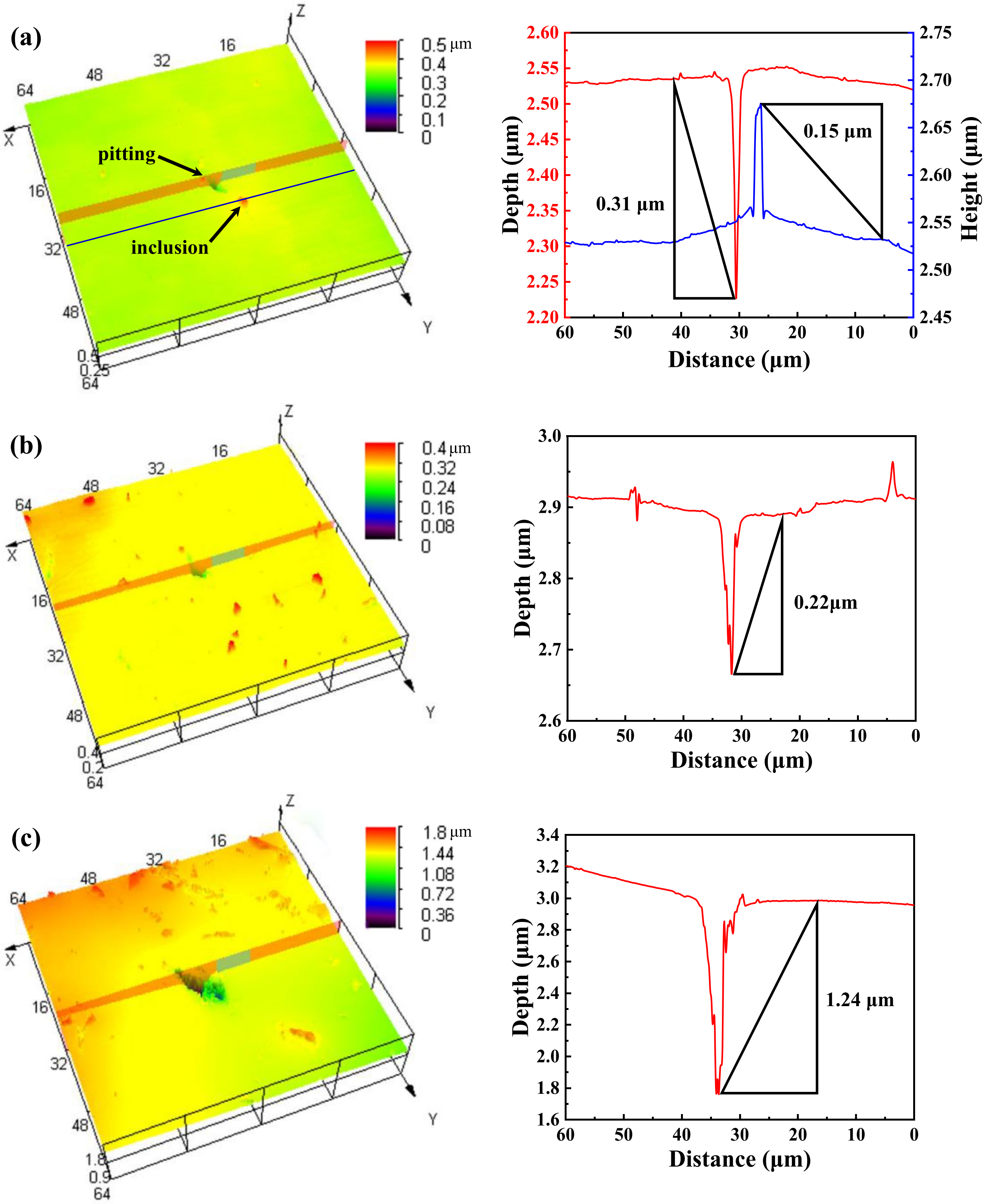

Fig. 6 Three-dimensional morphology of Ti-15–3 alloy samples after **a** 6 h, **b** 312 h, and **c** 720 h of the NSS test

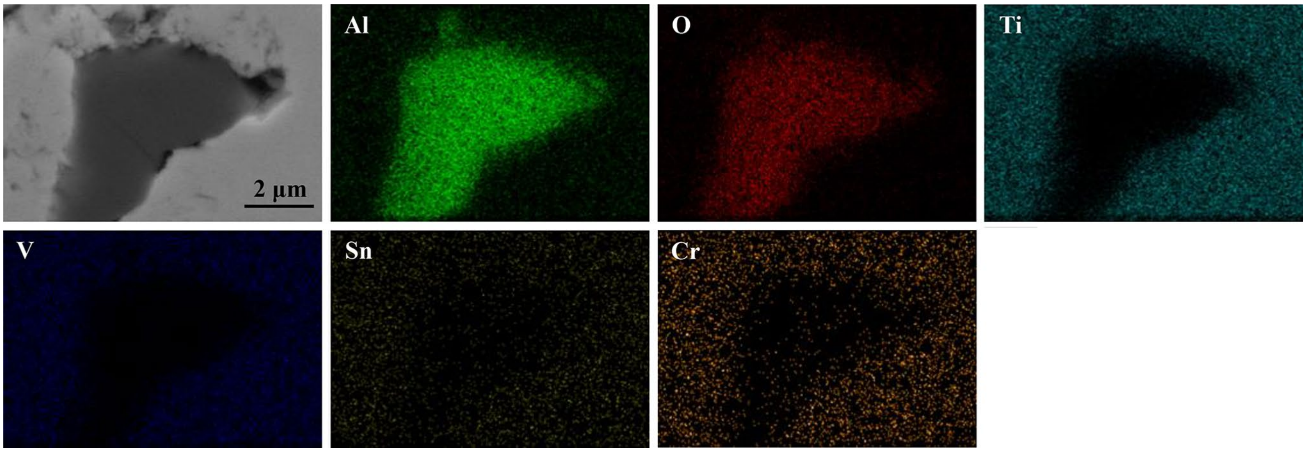

Fig. 7 Morphologies of the representative deposits with interstice of Ti-15–3 alloy sample after 312 h of NSS test and their corresponding elemental distribution results

of two contributions: the low binding energy peaks can be mainly attributed to the oxygen atom in TiO_2 lattice, while the higher binding energy peaks are mainly corresponding to the Ti-bonds of Me-OH(Ti–OH/Al–OH)/$Ti_2O_3(O_{Ti3+})$ [23]. The O 1 s spectra for Ti-15–3 alloy samples for 312 h and 720 h of salt spray can be mainly fitted to three different components: O^{2-} (~ 530.1 eV), Me-OH(Ti–OH/Al–OH)/Ti_2O_3 (~ 531.9 eV), and H_2O (~ 532.8 eV), this indicates that the corrosion product films are comprised of oxides, hydroxides, and hydrate.

The high-resolution spectrum of V $2p_{3/2}$ presented in Fig. 9d includes three peaks, where the first peak at 515.2 eV corresponds to V_2O_3 [24], the second peak at 516.3 eV corresponds to VO_2, and the last peak at 517.3 eV corresponds to V_2O_5 [25]. The V$2p_{1/2}$ spectrum includes two peaks, where one peak at 523.1 eV corresponds to VO_2 and another

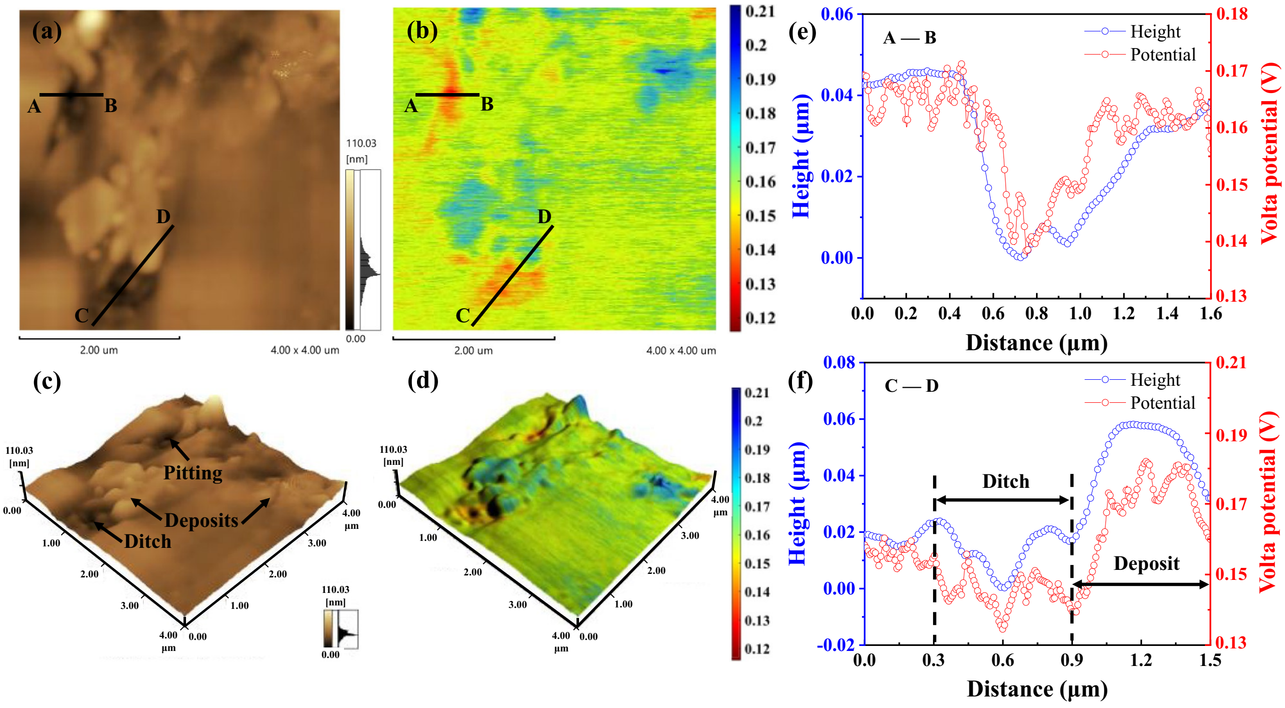

Fig. 8 SKPFM images of Ti-15–3 alloy sample after 312 h of the NSS test. **a** Surface topography and **b** potential distribution images; **c** 3D topography and **d** 3D Volta potential image of the selected target region; topography and Volta potential linear profiles recorded of **e** A-B and **f** C-D on **a** and **b** images, respectively

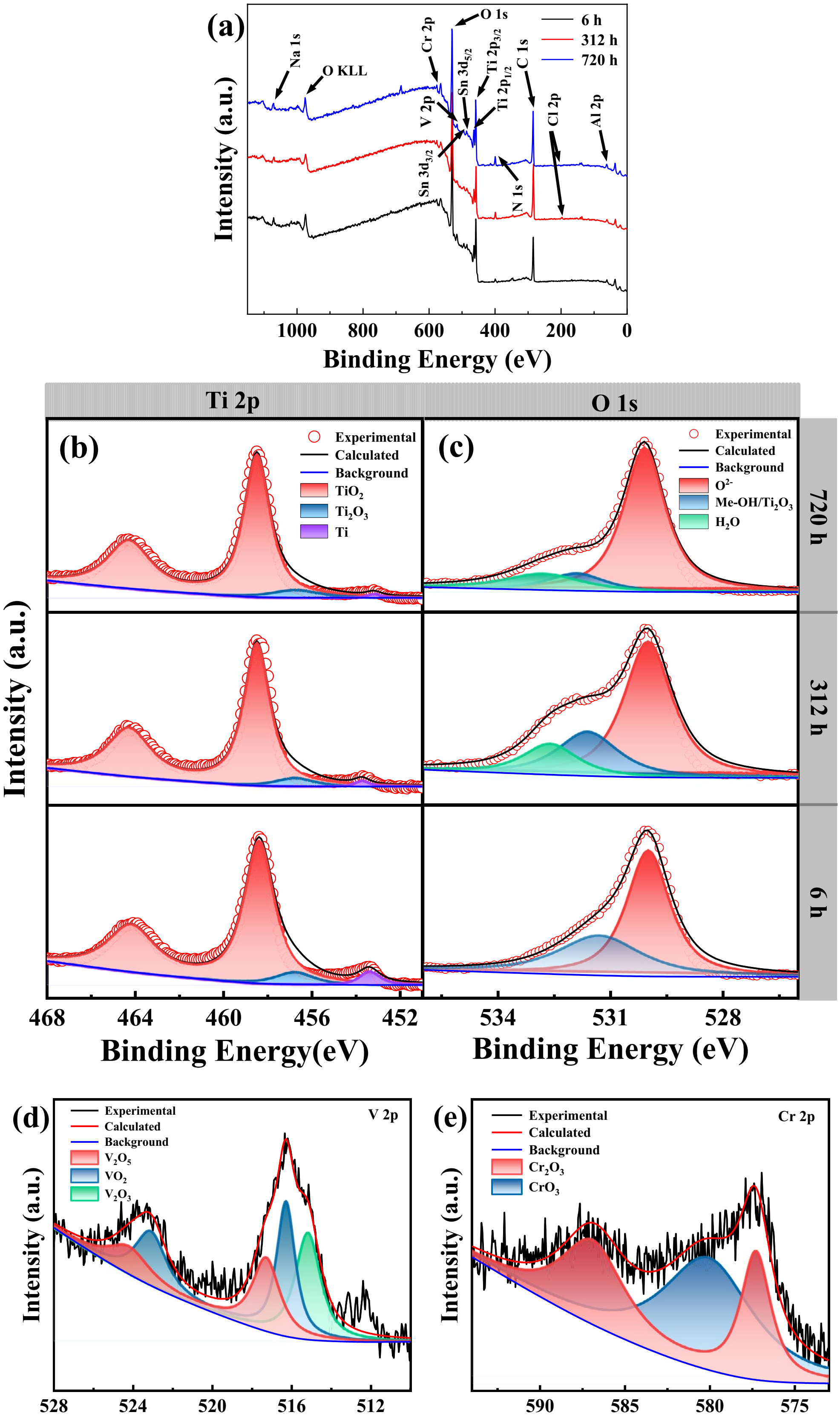

Fig. 9 Results of XPS measurements for Ti-15–3 alloys for different NSS time. **a** Typical survey spectra from XPS; detailed spectra from **b** Ti 2p, **c** O 1 s of Ti-15–3 alloys, **d** V 2p, **e** Cr 2p, **f** Al 2p, **g** Sn 3d, and **h** Cl 2p measured from the surface of Ti-15–3 alloy after 720 h of the NSS test

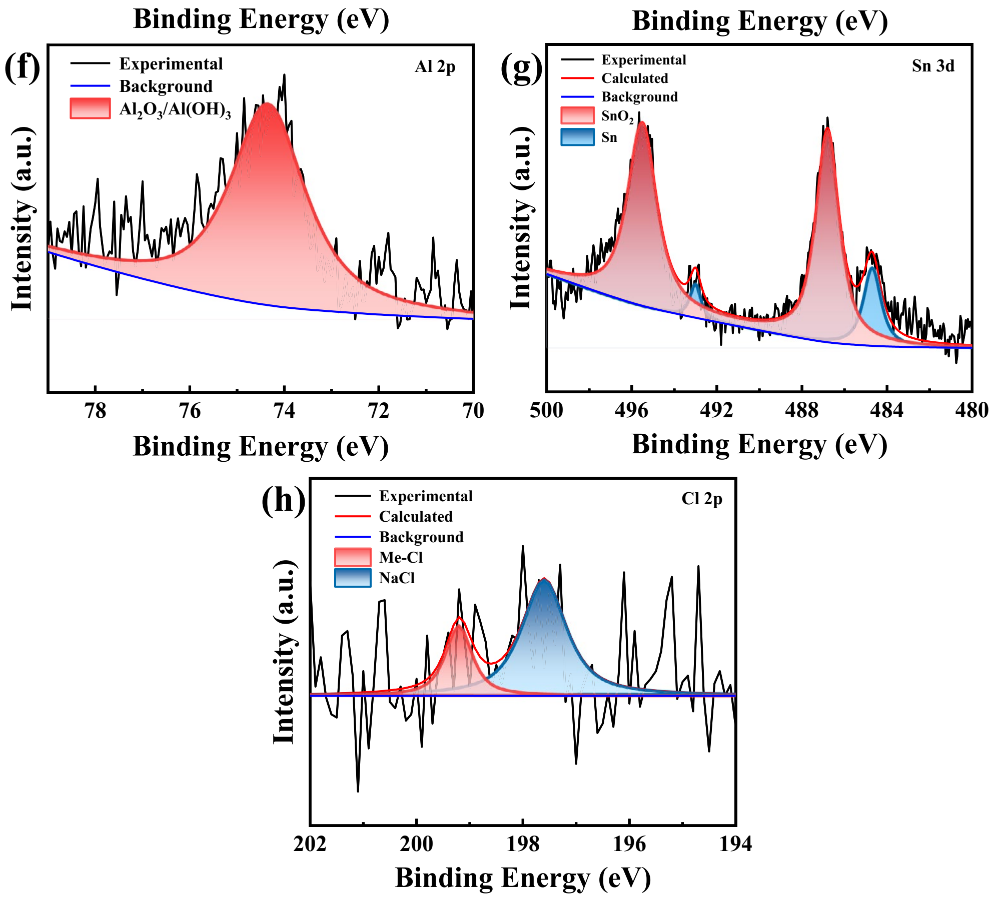

Fig. 9 (continued)

peak at 524.2 eV corresponds to V_2O_5. The high-resolution spectrum of $Cr2p_{3/2}$ presented in Fig. 9e contains two peaks, where one peak at 577.3 eV corresponds to Cr_2O_3 [26], and another peak at 580.1 eV corresponds to CrO_3. Moreover, a peak of the Cr $2p_{1/2}$ spectrum is observed at 586.9 eV, corresponding to Cr_2O_3, which can be assigned to the presence of Cr_2O_3 and CrO_3 in the corrosion product films. The formation of soluble CrO_3 is harmful, accelerating the dissolution of the oxide film [27]. As mapped in Fig. 9f, the peak in the Al 2p spectrum at 74.35 eV can be ascribed to the presence of Al_2O_3/$Al(OH)_3$. The high-resolution spectrum of Sn $3d_{5/2}$ presented in Fig. 9g includes two peaks at the binding energies of 484.7 eV and 486.8 eV, which can be attributed to Sn and Sn^{4+} (SnO_2) [26], respectively, suggesting that SnO_2 is formed with high content of 84.4 at.%.

The Cl 2p spectrum presented in Fig. 9h exhibits two main peaks, where one peak at 197.6 eV corresponds to NaCl and another peak at 199.2 eV corresponds to Me-Cl (Ti-Cl). In this study, the presence of $Al(OH)_3$/Ti–OH can illustrate the hydration reaction of the matrix during the salt spray test. The peak in Cl 2p spectrum at 199.2 eV can be ascribed to the presence of chloride in the corrosion product films. It can be believed that the $TiOHCl_x$ and $TiCl_x$ are formed on the surface of Ti-15–3 alloys in the salt spray for a long time.

OCP and electrochemical impedance spectroscopy (EIS)

In order to further elucidate the effect of salt spray time on the pitting resistance of Ti-15–3 alloy, electrochemical data were measured in a 3.5 wt.% NaCl solution. The corresponding open circuit potential (OCP), Nyquist, bode, and polarization resistance plots are presented in Fig. 10.

Figure 10a displays the OCP plots measured of Ti-15–3 alloy corroded by salt spray in a 3.5 wt.% NaCl solution. For 6 h of the NSS test, the OCP values of the Ti-15–3 alloy sample slowly rise from − 0.16 V/SCE to 0.13 V/SCE at the starting stage of ~ 1450 s and then stabilize at 0.14 V/SCE. The steady-state voltage values of the Ti-15–3 alloy sample for 72 h and 312 h of the NSS test are gradually shifted in a more positive direction, indicating that the anodic corrosion tendency is weakened, while the steady-state voltage value of the Ti-15–3 alloy sample for 720 h of the NSS test shifts

Fig. 10 **a** OCP, **b** Nyquist, **c** Bode-impedance moduli, and **d** bode-phase angles plots examined of Ti-15–3 alloy samples exposed to different NSS time in a 3.5 wt.% NaCl solution

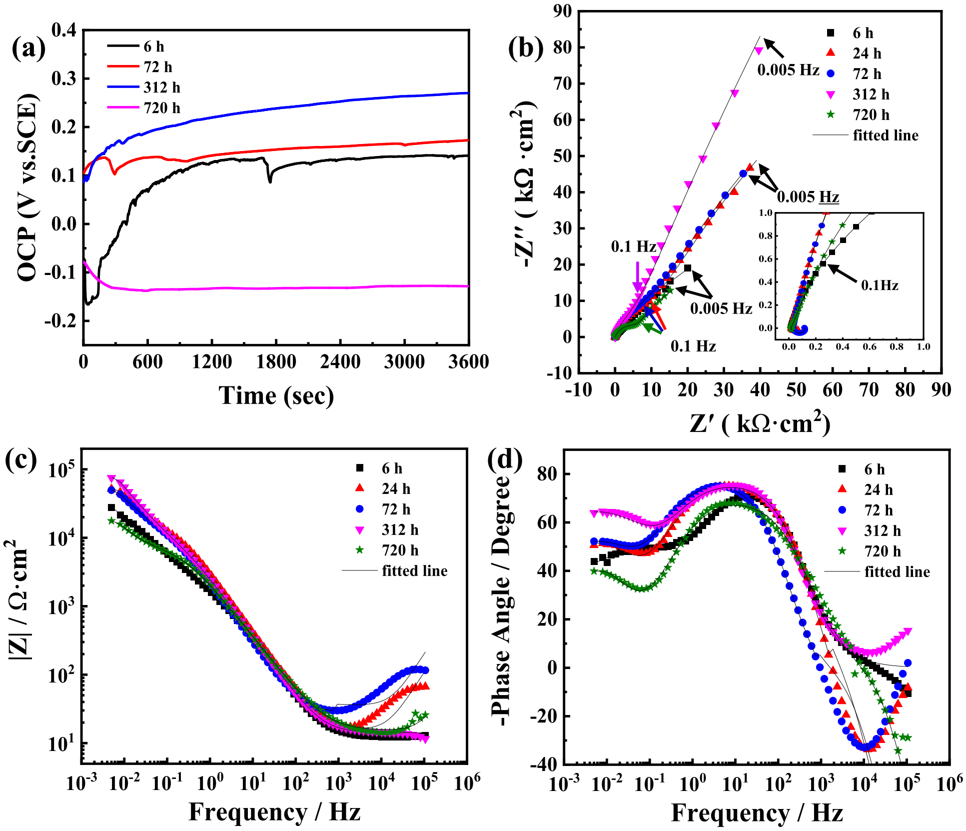

to a more negative direction, indicating that the stability of the oxide film surface becomes worse.

Figure 10b shows Nyquist plots measured of Ti-15–3 alloy corroded by salt spray in a 3.5 wt.% NaCl solution. All Nyquist plots show a small capacitive loop at high frequencies along with a big capacitive loop at low frequencies. The high-frequency capacitive loop can be related to the oxide film on alloy, and the low-frequency capacitive loop can be attributed to the passive layer related to charge transfer resistance at the passive film/alloy interface. By this time, the diameter of the capacitive loop stands for the resistance; in general, the resistance enhances with the increasing diameter of the arc [28]. Obviously, Fig. 10b shows that the low-frequency capacitive loops gradually increase in the range of 6 to 312 h, which implies an increase in salt spray time can cause the increase of corrosion resistance of Ti-15–3 alloys corroded by salt spray in 3.5 wt.% NaCl solution.

Regarding bode plots, the impedance moduli at the terminate frequency gradually increase in the range of 6 to 312 h (Fig. 10c), indicating that the corrosion resistance can be enhanced by an increasingly stable passive film. However, for 720 h of NSS, the impedance modulus at the terminate frequency reduces suddenly, manifesting rapid cation release at the film/solution interface and continuous propagation of the pitting corrosion. Moreover, for Fig. 10d, bode-phase angle plots contain two peaks, suggesting the appearance of two-time constants [29]. It is worth noting that the maxima of phase angle curves in bode plots are all less than 90°, which suggests that a deviation of ideal capacitance appears relative to the electrochemical interface.

To further interpret the corrosion behavior of Ti-15–3 alloys corroded by salt spray, an equivalent circuit with two-time constants according to Fig. 11 is used to fit the impedance data [30]. Hence, the charge transfer controlled phenomenon exists in electrochemical reactions. In the Nyquist plot. In addition to charge transfer resistance (R_{ct}), there is still film resistance (R_f) that is ascribed to the protective film on the metal surface. Furthermore, in this equivalent circuit, R_s is the solution resistance. Z_W is a finite length Warburg impedance element that represents the diffusion of reactive species [31, 32]. Herein, a constant phase element (CPE) was used to describe the double layer capacitance (CPE_{dl}) and film capacitance (CPE_f) due to dispersion effects which derive from surface heterogeneities [33, 34]. The impedance of CPE can be defined as follows:

$$Z_{CPE} = \frac{1}{Q}(jw)^{-n} \tag{1}$$

where Q is the magnitude of the CPE; ω is the radian frequency; and n is the deviation parameter ($0.5 \leq n \leq 1$, which

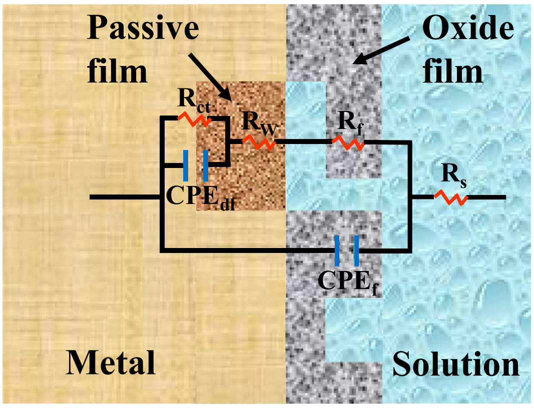

Fig. 11 The equivalent electrical circuits used for fitting impedance data for different NSS time

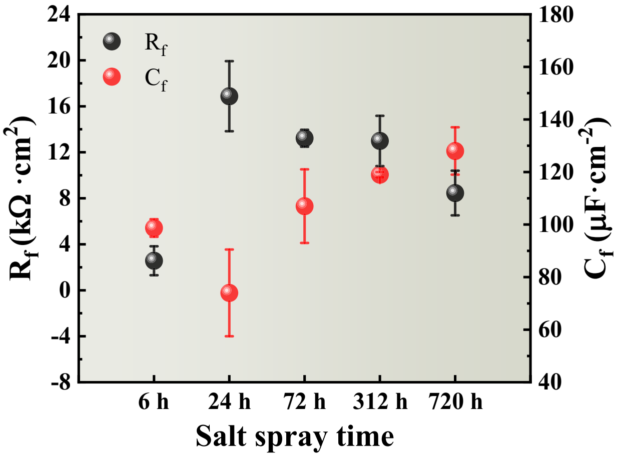

Fig. 12 R_f-C_f values of Ti-15–3 alloy samples exposed to different NSS time. These were calculated using the EIS data in Fig. 10

is often called the dispersion exponent because of the heterogeneity or the roughness of the alloy surface) [35, 36]. In this electrical circuit, CPE_{dl} is connected in parallel with R_{ct} and CPE_f is associated with R_f, which is further joined with the diffusion resistance (R_W) and solution resistance (R_s) through a series of combination. The EIS spectra measured in 3.5 wt.% NaCl solution can be well fitted using an equivalent circuit with a two-time constant (Fig. 11), and the detailed EIS fitting data are presented in Table 2. All chi-square (χ^2) values are nearly less than 0.01, indicating a high fitting degree.

On the basis of the report by Liu et al. [30], total resistance R_p, which is inversely proportional to the corrosion rate, for all NSS time, the R_p is given by the total of the charge transfer resistance (R_{ct}), the oxide film resistance (R_f), and R_W as follows: $R_p = R_{ct} + R_f + R_W$.

According to Table 2 and Fig. 12, the values of R_f rapidly increase and then decrease with increasing salt spray time; correspondingly, the values of C_f firstly decrease and then exhibit a drastic increase of the capacitance C_f. Specifically, the C_f values for Ti-15–3 alloy continuously increase over 24 h of the NSS test, which be attributed to the degradation of oxide film due to the penetration of the electrolyte through the oxide film pores. The effective capacitance associated with the CPE of the oxide film for a distribution in the direction perpendicular to the electrode interface with diffusion can be denoted as follows:

$$C_f = \left[CPE_f(R_f + R_{ct} + R_{W_0})^{1-n_f}\right]^{\frac{1}{n_f}} \tag{2}$$

where C_f is the oxide film capacitance. This equation follows the development of the film capacitance formula introduced by Hirschorn et al. [35].

The thickness of an oxide film, d_f, can be acquired by the following formula [37–39]:

$$d_f = \frac{\varepsilon_0 \varepsilon A}{C_f} \tag{3}$$

where d_f is the thickness of the oxide film, ε_0 is the vacuum permittivity (8.8542×10^{-14} F·cm^{-1}), and A is the surface

Table 2 The fitted electrochemical impedance parameters of Ti-15–3 alloys for different NSS time in a 3.5 wt.% NaCl solution

Corrosion time	6 h	24 h	72 h	312 h	720 h
R_s(Ω·cm^2)	12.31	16.46	29.2	14.26	14.46
CPE_f (Ω^{-1}·cm^{-2}·s^{nf})	8.53×10^{-5}	6.36×10^{-5}	8.48×10^{-5}	8.54×10^{-5}	1.04×10^{-4}
n_f	0.86	0.88	0.89	0.85	0.79
R_f (Ω·cm^2)	2567	16,877	13,221	12,985	8457
C_f (F·cm^{-2})	9.87×10^{-5}	7.40×10^{-5}	1.07×10^{-4}	1.19×10^{-4}	1.28×10^{-4}
R_w (Ω·cm^2)	0.26	0.46	0.18	17,812	0.16
CPE_{dl} (Ω^{-1}·cm^{-2}·s^{ndl})	2.88×10^{-4}	2.57×10^{-4}	1.22×10^{-3}	5.60×10^{-4}	1.19×10^{-3}
n_{dl}	0.61	0.82	0.92	0.95	0.89
R_{ct} (Ω·cm^2)	22,523	42,712	48,478	57,486	15,228
R_p (Ω·cm^2)	25,090.26	59,589.46	61,699.18	88,283	23,685.16
χ^2	2.34×10^{-4}	2.25×10^{-3}	1.65×10^{-3}	3.81×10^{-3}	1.68×10^{-3}

area, ε is the relative dielectric constant of the oxide film. Generally, the oxide film formed on titanium is rutile; thus, ε can be assumed to be 65 [29, 40].

Because A and ε_0 are constant before pitting corrosion, any changes in C_f come from either change in d_f or ε variation [41]. However, when pitting corrosion occurs, the area of the passivated surface usually decreases with salt spray time because of active corrosion of the pitted area. Although the actual value of ε within the film is difficult to estimate, the magnitude of capacitance C_f can be considered as an indicator for the thickness of the oxide film [39]. In this study, the changes of ε with time are assumed to be neglected. Therefore, the capacitance C_f of the surface oxide film is inversely proportional to its thickness.

As seen in Table 2, the values of R_{ct} were significantly higher than those of R_f for all the NSS time. Hence, it turns out that the value of R_{ct} can determine the corrosion resistance of the corroded sample. Figure 13 shows that the change regular of R_{ct} and R_p values was similar. R_{ct} increases from 22523·to 57486 Ω·cm^2 when the salt spray time increases from 6 to 312 h.This can be ascribed to the thickened passive film. Specifically, the R_p value for the Ti-15–3 alloy sample is considerably large at 312 h of the NSS test, i.e. approximately 88.28 kΩ·cm^2, but the R_p value suddenly reduces to about 23.69 kΩ·cm^2 for 720 h, indicating that its corrosion resistance is weakened. After 720 h of the NSS test, the weakening of the corrosion resistance can be also reflected in the increase in CPE_{dl} value, which can be ascribed to the reduction of double-layer thickness because of the increase of defects (e.g. holes) in the passive film [32].

Electrochemical noise

Potential and current transients

To complete the study on the pitting corrosion behavior of Ti-15–3 alloy samples exposed to different salt spray time, the EN test was performed to study the electrochemical potential and current noise transients analyses in a 3.5 wt.% NaCl solution. The typical electrochemical potential and current noises recorded of Ti-15–3 alloy samples corrode by different NSS time in 3.5 wt.% NaCl solution is presented in Fig. 14. For pitting corrosion, the features of electrochemical noise transients directly reveal processes occurring in the associated pits [42]. As shown in Fig. 14a, there appear two transient peaks with a long lifetime (200 s) for 6 h of the NSS test at test time regions between 1800 and 2400 s. However, the direction of the current transients only indicates that one of the working electrodes suffers a local attack, and thus, the current transients of a small icon in Fig. 14a exhibit an increasing rise towards their maximum absolute values. As shown in a small icon from Fig. 14a, the current transient is characterized by a rapid rise and then slow recovery; those current transients were produced by the formation of stable pitting caused by acidification at the oxide film/metal matrix interface due to the attack of chloride ions [43].

Compared with the curves in Fig. 14a, b shows that the initiation rate (the number of current peaks per hour) for 72 h of the NSS test increases. Nevertheless, this increase is not because salt spray corrosion accelerates the growth of stable pitting, but because of the failure of the cathodic protective effect of growing pits. Hence, once a pit is rapidly passivated, a new metastable pitting will initiate because of the attack of the chloride ion. It is believed that rapid growth and death of metastable pitting may lead to an increase in nucleation rate in such case [44]. Two small icons in Fig. 14b show the amplifying curves of transients from the black and red boxed regions. It is interesting to note that the current transient from the black-boxed region is characterized by a fast rise and then rapid drop, meaning that a metastable event from generation to repair of the metastable pitting [45]. However, the current transients from the red boxed region are characterized by a rapid rise and then slow recovery lasting a long time; meanwhile, in the process of the attenuation for the current transient peak, many secondary noise peaks with a short lifetime and small amplitude appear, which may be related to the nucleation mechanism that the formation of stable pitting can promote the initiation rate of metastable pits [12].

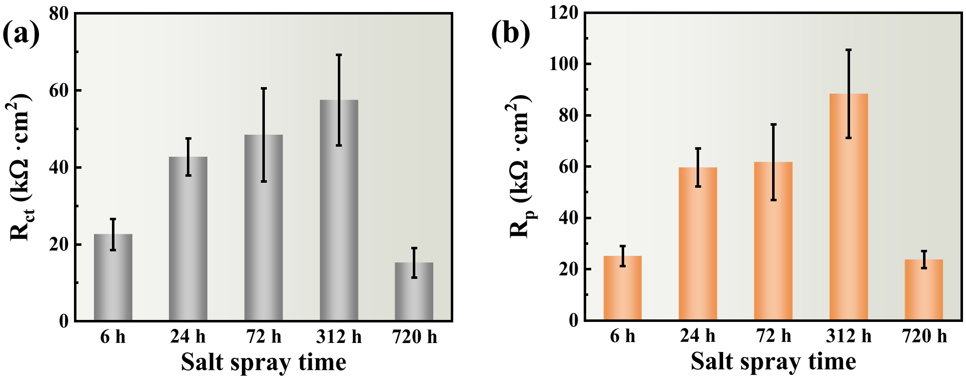

Fig. 13 **a** R_{ct} and **b** R_p values of Ti-15–3 alloy samples exposed to different NSS time. These were calculated using the EIS data in Fig. 10

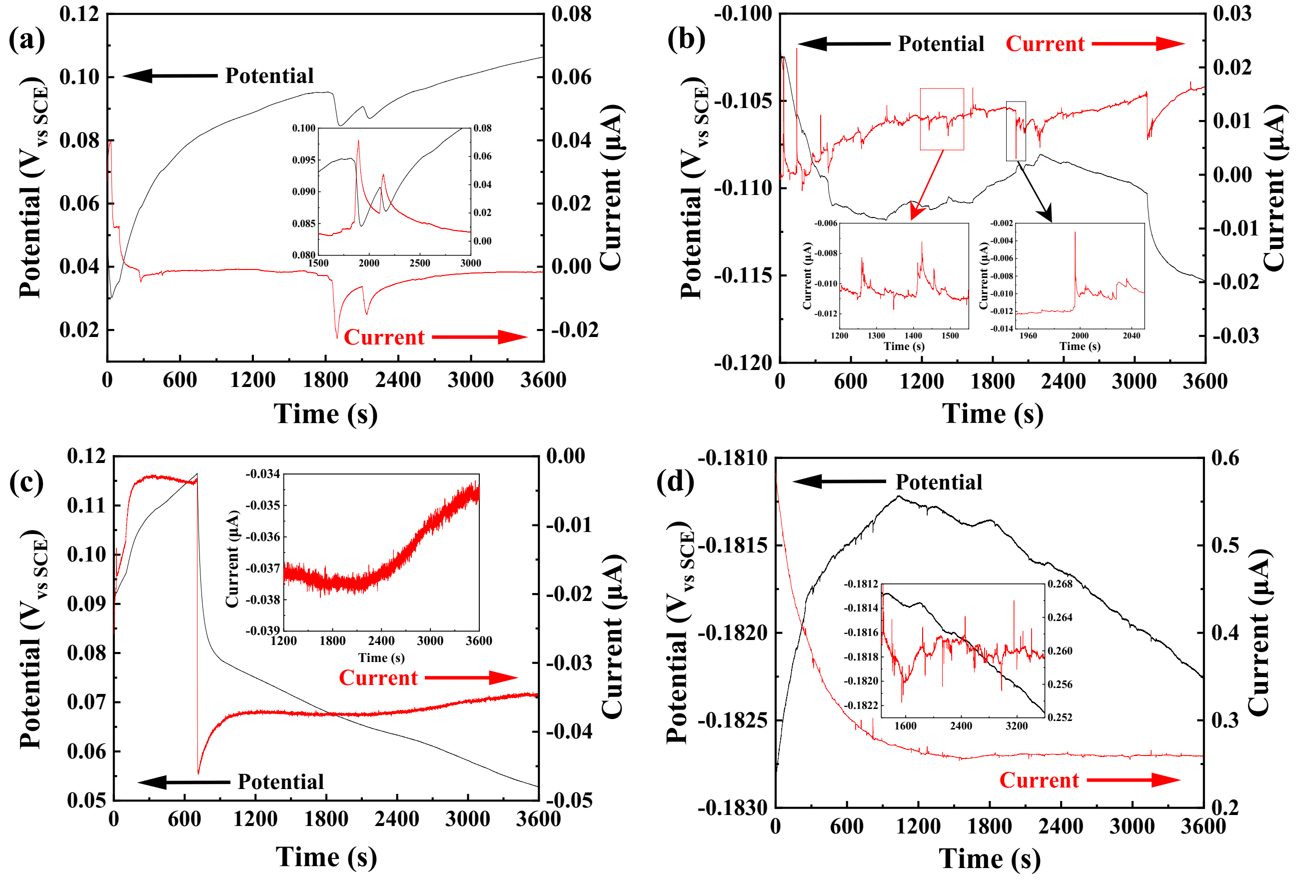

Fig. 14 The current and potential EN data examined of Ti-15–3 alloy samples exposed to **a** 6 h, **b** 72 h, **c** 312 h, and **d** 720 h to salt spray in a 3.5 wt.% NaCl solution

From Fig. 14c, it can be seen that the number of the large current transients for 312 h of the NSS test markedly decreases when compared with that in Fig. 14b. There appears a transient peak at about 710 s, which is the feature of fast rise and slow recovery. Subsequently, a small icon in Fig. 14c shows the feature of the cluster transients. It is thought that the cluster transients are caused by repeated dissolution around the same site [46]. In general, during the repassivation process of stable pitting, the areas around the stable pitting site are unstable and are also preferential sites for the following metastable pitting events [47].

Especially, for 720 h of the NSS test, not only the baseline of current–time curve increases by 26 times, but the nucleation events markedly increase when compared with Fig. 14a, and a large-scale negative shift of average potential from 0.09 V vs. SCE to – 0.11 V vs. SCE (Fig. 14d), indicating the formation of an increasing number of stable pitting. Indeed, many pitting corrosions appear on the surface of the Ti-15–3 alloy sample, as shown in Fig. 4d.

Evaluation of spectral noise resistance

As shown in Fig. 15a, Spectral noise resistance is defined as the square root of the potential PSD divided by the current PSD [48]. During the 312 h of salt spray, the R_{sn} values at very low frequencies (below 1 mHz) gradually increase with lengthening salt spray time, indicating that the formative passive film enhanced the corrosion resistance of Ti-15–3 alloy. On day 30, the R_{sn} values at very low frequencies are almost tow orders of magnitude smaller than those for 312 h of salt spray. Figure 15b shows comparing the results of the spectral noise resistance (R_{sn}) and the modulus |Z| of the impedance. Comparing the values of $|Z|_{10}{}^{-2}$ Hz and R_{sn} of the polished Ti-15–3 alloy electrodes after different salt spray time, a similar tendency can be seen. All R_{sn} curves lie above the |Z| curves, from 6 to 312 h of salt spray, the R_{sn} values are an order of magnitude higher than the modulus of the impedance at low frequency. For 720 h of salt spray, the R_{sn} values are very close to the modulus of the impedance

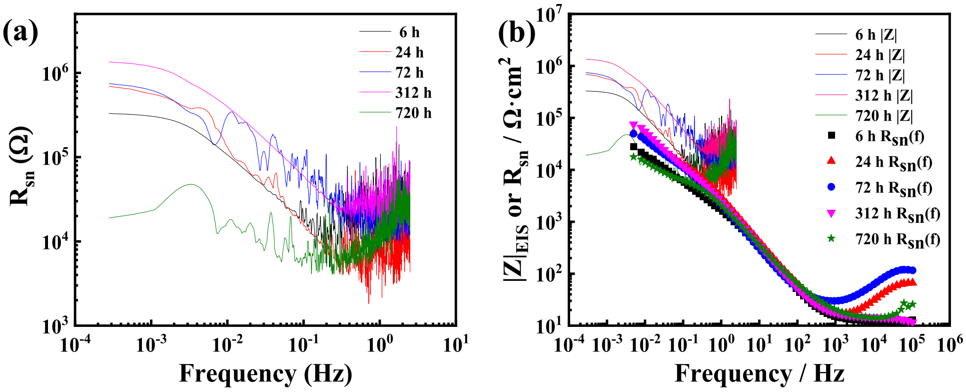

Fig. 15 **a** The spectral noise resistance plots of Ti-15–3 alloys after different salt spray time; **b** comparison results between |Z| and R_{sn} of Ti-15–3 alloys with different surface states after different salt spray time

at low frequency. These differences can be generally attributed to the sensibility of the EN technique [49].

Hilbert-Huang transform analysis

Hilbert spectra of EPN signals of Ti-15–3 alloy samples exposed to different salt spray time are shown in Fig. 16. For HHT analyses, it is widely accepted that the high contribution of the EPN spectra in high-frequency (10^{-1}–10^{0}) and low-frequency (10^{-4}–10^{-1}) can successively reflect information about a passive state or growth or death of metastable pitting and the growth of stable pitting. As shown in Fig. 16a, the Hilbert spectrum of the EPN signal of Ti-15–3 alloy after 6 h of the NSS test shows the presence of low instantaneous frequencies (below 10^{-2} Hz) only in the range of 500 to 2000s, meaning a large time scale phenomenon is going on. This indicates relatively localized activity [17]. This result of the analysis is in accordance with the analysis of the inset marked in Fig. 14a. Figure 5a shows that the characteristic localized attacks form on the surface of Ti-15–3 alloy at 6 h of the NSS test.

For 72 h of the NSS test, the Hilbert spectrum of the Ti-15–3 alloy sample exhibits high contribution of spectrum in low-frequency regions below 10^{-1} Hz, which is influenced to a large extent by the large potential drop. A slight contribution of the spectrum can clearly be seen in high-frequency regions above 10^{-1} Hz (as marked by the red arrow in Fig. 16b), Combined with the very small DC value of the ECN signals (Fig. 14b), these data indicate a slow transition to a passive state [50].

For 312 h of the NSS test, only a instantaneous peak is observed in Fig. 14c, lots of low amplitude fluctuations

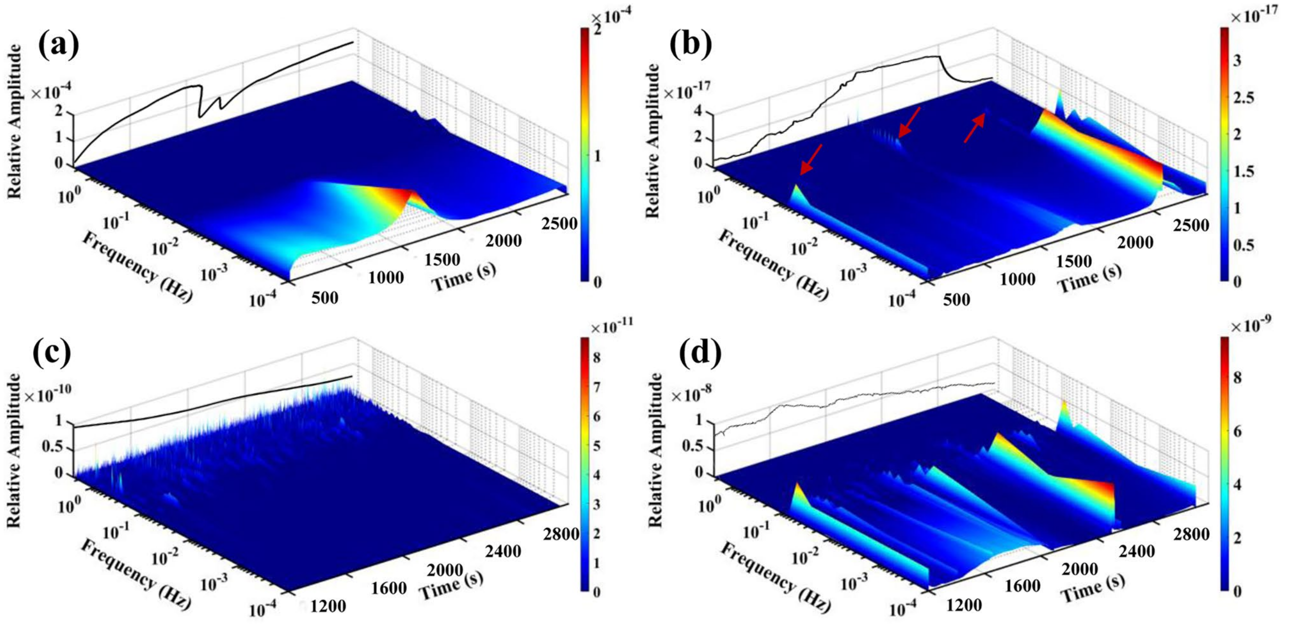

Fig. 16 Hilbert spectra of EPN signal for **a** 6 h, **b** 72 h, **c** 312 h, and **d** 720 h to salt spray. These were calculated using the electrochemical noise data in Fig. 14

appear after about 900 s. To investigate this small invisible transient, only the Hilbert spectrum of the EPN signal after 1200 s was generated, without the influence of the large low-frequency part. Accordingly, a uniformly distributed energy contribution of the spectra in high-frequency regions above 10^{-1} Hz along the entire measurement is observed (Fig. 16c), indicating a white noise type of energy distribution. Actually, a white noise type of spectrum over the whole high-frequency domain indicates whether the process is active or passive. But, the EPN signal is almost straight and smooth, primarily consisting of a DC drift component, combined with the very small DC value of the ECN signals, these data indicate a slow transition to a passive state [19, 51]. R_p from Fig. 13b verifies these results, Microscopic observation from Fig. 5c shows the widths of both pitting corrosions and ditches on the surface remain about 2 mm when compared with those in Fig. 5a and b. Hence, the pitting corrosion had not actively propagated but remained in a passive state at longer salt spray time.

For 720 h of the NSS test, lots of characteristic peaks appear after 1200 s, as shown by the small icon in Fig. 14d. To research these transient peaks, only the EPN Hilbert spectrum after 1200 s was generated, without the influence of the DC part at 1200 s before (Fig. 14d). Therefore, high distribution of the spectra is observed only in low-frequency regions below 10^{-1} Hz (Fig. 16d), indicating the formation of large amounts of stable pitting [17]. The presented macrographs from Fig. 5d and CLSM analysis from Fig. 6c and d show the propagation and evolution of pitting corrosions.

Discussion

Mechanisms of oxide film rupture of Ti-15–3 alloy in Salt spray

After analyzing 3D morphology, 3D Volta potential map, and chemical composition at various corrosion time, the schematic diagram with various reactions of corrosion behavior for Ti-15–3 alloy in the salt spray is shown in Fig. 17. From Fig. 3, native oxide films of the polished Ti-15–3 alloy are mainly composed of TiO_2, V_2O_5, Cr_2O_3, Al_2O_3, and SnO_2.

According to SEM observation (see Fig. 5), CLSM calculation (see Fig. 6), EDS analysis (see Fig. 7), and SKPFM measurement (Fig. 8), the salt spray corrosion process can be mainly divided into two types of corrosion behavior, as shown in Fig. 17. Type I is the local dissolution of air-formed oxide film on Ti-15–3 alloy surface, resulting in the formation of pitting corrosion once the oxide film is destroyed. Type II is the preferential dissolution of metal matrix around deposits, leading to the formation of a ditch due to high deformation [20]. Meanwhile, since heterogeneous oxide film are prone to break down in salt spray environment, local deposits (Al_2O_3) can be formed in contact with aqueous solutions (Fig. 9f):

$$2A1 + 3H_2O \rightarrow Al_2O_3 + 6H^+ + 6e^- \tag{4}$$

Thereby, the interface between deposits and matrix always acts as a site to be destroyed due to the existence of the adsorption of Cl^- and high distortion. Herein, the metal as an anode is dissolved, while dissolved oxygen acts as a deoxidizer. As a result, ditches at the deposit/metal interface are inevitably generated (see Fig. 5).

In short, two types of corrosion behavior both are the dissolution of the matrix: type I is the cavities and type II is some ditches around the deposit (see Figs. 5 and 8). Some researchers have found that the pit takes place through the dissolution of Ti in the form of Ti^{4+} [52]. With the increase in the concentration of metal cations within the pit, the Cl^- outside the pit migrates in to maintain electrical neutrality. The resulting autocatalytic cell and oxygen-concentration cell are gradually formed, accelerating the dissolution of the metal matrix. The electrochemical reactions at this stage are as follows [53]:

$$Ti + H_2O \leftrightarrow (TiOH)_{ad} + H^+ + e^- \tag{5}$$

$$(TiOH)_{ad} \leftrightarrow (TiOH)^{x+} + xe^- \tag{6}$$

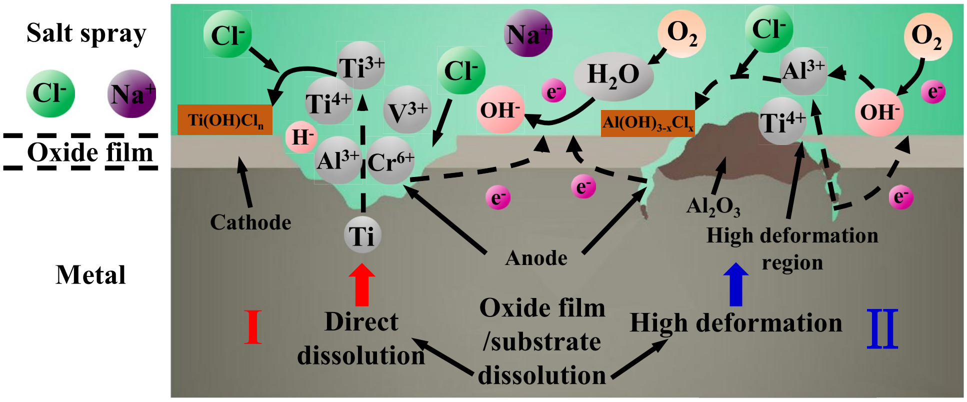

Fig. 17 The schematic diagram of corrosion behavior of Ti-15–3 alloy sample in salt spray

Then, $(TiOH)^{x+}$ is dissolved to soluble $Ti(OH)Cl_x$ species in the local acidified environment (see Fig. 9c and h), Possible reactions are given as follows:

$$(TiOH)^{x+} + H^+ \leftrightarrow Ti^{x+} + H_2O \tag{7}$$

As is well known, metallic Ti, Al, V, and Cr are accessible oxidation. Hence, when the bare metal are exposed to salt spray, the active metal atoms will easily react with H_2O or Cl^-.

Effect of the salt spray test time on corrosion behavior of Ti-15–3 alloy

According to surface topography and current transient (see Fig. 14a), the native oxide film on the Ti-15–3 alloy surface at the initial stage of salt spray was damaged, accompanied by the formation of localized corrosion. As shown in Fig. 16a, the result of the Hilbert spectrum analysis also confirms that relatively localized activities appear on the surface of Ti-15–3 alloy.

The results of the Hilbert spectrum analysis in Fig. 16c reveal the development of a passive process on the Ti-15–3 alloy surface in the middle of salt spray, combining with the further electrode/solution interface analysis of the EIS (Fig. 10), indicating that the inner dense passive film plays a key role to protect alloy matrix from corrosion after the native oxide film was damaged. The R_{ct} values from Fig. 13a prove the increase in corrosion resistance of the inner passive film. Furthermore, the polarization resistance (see Fig. 13b) and R_{sn} analyses (see Fig. 15a) reveal a smaller corrosion rate in the middle of salt spray, implying that the anodic reaction of bare metal can be restrained due to the replenishment of oxygen and the formation of a more stable passive film. At this moment, the passivation within the pitting may occur [54]:

$$Me + H_2O \leftrightarrow (MeOH)_{ad} + H^+e^- \tag{8}$$

$$(MeOH)_{ad} + H_2O \rightarrow [Me(OH)_x]_{ad} + H^+ + e^- \tag{9}$$

$$[Me(OH)_X]_{ad} \rightarrow Me_yO_{xfilm} + H^+ + e^-(Me_yO_x \text{ contains } TiO_2, V_2O_5, Cr_2O_3, Al_2O_3, SnO_2) \tag{10}$$

During this process, the dissolution of the bare metal ejected Ti^{4+} cations through the crack of the passive film. Meanwhile, the hydrate ($TiO_2 \cdot nH_2O$) is formed by the hydrolysis of $Ti^{4+}{}_{aq}$ cations, which can enhance the resistance of the passive film to the attack of chloride ions. The result of the XPS analysis also proves the formation of the hydrate group (see Fig. 9c), the reaction can be given below [55]:

$$TiO_2(film) + 4H^+ \rightarrow Ti^{4+}{}_{aq} + 2H_2O \tag{11}$$

$$Ti^{4+}{}_{aq} + (n+2)H_2O \rightarrow TiO_2nH_2O + 4H^+ \tag{12}$$

Combined with surface topography and Hilbert spectrum analysis (see Fig. 16d), at the later stage of salt spray, Ti-15–3 alloy sample surface after salt spray corrosion was undergoing the growth of stable pitting, accompanied by a rupture of the oxide film and/or passive film, and further dissolution of the metal matrix. R_f and C_f values from Fig. 11 prove the degradation of the native oxide film, and the polarization resistance (see Fig. 13b) and R_{sn} analyses (see Fig. 15a) also reveal the weakening of the corrosion resistance. According to the XPS analysis (Fig. 9), the dissolution reaction of the passive film can be expressed as follows [55]:

$$\begin{aligned} &Me_{n-1}O_{nfilm} + 2nH^+ \rightarrow Me^{2n+} \\ &\quad + nH_2O(Me_{n-1}O_{nfilm} contains TiO_2, SnO_2) \end{aligned} \tag{13}$$

$$\begin{aligned} &Me_mO_{nfilm} + 2nH^+ \rightarrow mMe^{n+} \\ &\quad + nH_2O(Me_mO_n contains V_2O_5, Cr_2O_3, Al_2O_3 \end{aligned} \tag{14}$$

Conclusions

Microstructure characteristic, pitting behavior, and pitting resistance of Ti-15–3 alloy in a salt spray environment have been evaluated. The main conclusions of this study are as follows:

(1) The R_{sn} calculated using the fast Fourier transform has consistent analytical results with the impedance |Z| modulus obtained from the EIS test. The R_{sn} value at the termination frequency and R_p value reflects the severity of corrosion.

(2) The Hilbert spectra based on the Hilbert-Huang transform of the potential noises can act as the fingerprints to identify the form in which the system under the salt spray test corrodes. The corrosion forms of Ti-15–3 alloy samples after different salt spray time are localized corrosion, self-healing of passive film and nucleation, and growth of new pitting corrosion.

(3) Based on the observation of surface morphology, the complementary evaluation of corrosion rate, and the

Hilbert spectrum, it is found that both the pitting corrosions and ditches with a width of about 2 mm on the surface of polished Ti-15–3 alloy before 720-h salt spray are less vulnerable to cause the formation of stable pitting, while the pit with the width of about 5 mm on polished Ti-15–3 alloy surface after the 720-h salt spray is prone to the growth of stable pitting.

(4) According to SEM and CLSM-3D morphology observation as well as EDS and SKPFM analyses, there are two mechanisms for the oxide film rupture of polished Ti-15–3 alloy surface in the process of salt spray corrosion: the first is the local dissolution of natural oxide film on the surface of Ti-15–3 alloy and the second is the preferential dissolution of metal matrix around the deposit.

Acknowledgements The present work was supported by the LiaoNing Revitalization Talents Program, China (No. XLYC1902084).

Declarations

Competing interest The authors declare no competing interests.

References

1. Tan MJ, Zhu X, Thiruvarudchelvan S, Liew K (2008) Superplasticity studies in a beta titanium alloy. Arch Mater Sci Eng 28
2. Otieno M, Beushausen H, Alexander M (2016) Chloride-induced corrosion of steel in cracked concrete—Part II: Corrosion rate prediction models. Cem Concr Res 79:386–394. https://doi.org/10.1016/j.cemconres.2015.08.008
3. Neves R, Silva A, de Brito J, Silva RV (2018) Statistical modelling of the resistance to chloride penetration in concrete with recycled aggregates. Constr Build Mater 182:550–560. https://doi.org/10.1016/j.conbuildmat.2018.06.125
4. Frankel GS (1998) Pitting corrosion of metals: a review of the critical factors. J Electrochem Soc 145:2186. https://doi.org/10.1149/1.1838615
5. Bhandari J, Khan F, Abbassi R et al (2015) Modelling of pitting corrosion in marine and offshore steel structures – a technical review. J Loss Prev Process Ind 37:39–62. https://doi.org/10.1016/j.jlp.2015.06.008
6. Kolman DG, Scully JR (1994) Electrochemistry and passivity of Ti-15 V-3 Cr-3 Al-3 Sn β-titanium alloy in ambient temperature aqueous chloride solutions. J Electrochem Soc 141:2633. https://doi.org/10.1149/1.2059146
7. Sun Z, He G, Meng Q et al (2020) Corrosion mechanism investigation of TiN/Ti coating and TC4 alloy for aircraft compressor application. Chin J Aeronaut 33:1824–1835. https://doi.org/10.1016/j.cja.2019.08.015
8. Xie L, Zhou W, Zou S (2021) Pitting behavior of Ti-15-3 titanium alloy with different surface in salt spray studied using electrochemical noise. J Mater Res Technol 14:2865–2883. https://doi.org/10.1016/j.jmrt.2021.08.072
9. Calabrese L, Bonaccorsi L, Galeano M et al (2015) Identification of damage evolution during SCC on 17–4 PH stainless steel by combining electrochemical noise and acoustic emission techniques. Corros Sci 98:573–584. https://doi.org/10.1016/j.corsci.2015.05.063
10. Legat A, Zevnik C (1993) The electrochemical noise of mild and stainless steel in various water solutions. Corros Sci 35:1661–1666. https://doi.org/10.1016/0010-938X(93)90396-X
11. Shi Z, Song G, Cao C et al (2007) Electrochemical potential noise of 321 stainless steel stressed under constant strain rate testing conditions. Electrochim Acta 52:2123–2133. https://doi.org/10.1016/j.electacta.2006.08.029
12. Dong ZH, Shi W, Guo XP (2011) Initiation and repassivation of pitting corrosion of carbon steel in carbonated concrete pore solution. Corros Sci 53:1322–1330. https://doi.org/10.1016/j.corsci.2010.12.028
13. Huang NE, Shen Z, Long SR et al (1998) The empirical mode decomposition and the Hilbert spectrum for nonlinear and nonstationary time series analysis. Proc R Soc Lond Ser Math Phys Eng Sci 454:903–995. https://doi.org/10.1098/rspa.1998.0193
14. Huang NE, Wu M-LC, Long SR et al (2003) A confidence limit for the empirical mode decomposition and Hilbert spectral analysis. Proc R Soc Lond Ser Math Phys Eng Sci 459:2317–2345. https://doi.org/10.1098/rspa.2003.1123
15. Feldman M (2011) Hilbert transform in vibration analysis. Mech Syst Signal Process 25:735–802. https://doi.org/10.1016/j.ymssp.2010.07.018
16. Homborg AM, Leon Morales CF, Tinga T et al (2014) Detection of microbiologically influenced corrosion by electrochemical noise transients. Electrochim Acta 136:223–232. https://doi.org/10.1016/j.electacta.2014.05.102
17. Hoseinieh SM, Homborg AM, Shahrabi T et al (2016) A novel approach for the evaluation of under deposit corrosion in marine environments using combined analysis by electrochemical impedance spectroscopy and electrochemical noise. Electrochim Acta 217:226–241. https://doi.org/10.1016/j.electacta.2016.08.146
18. Cook AB, Barrett Z, Lyon SB et al (2012) Calibration of the scanning Kelvin probe force microscope under controlled environmental conditions. Electrochim Acta 66:100–105. https://doi.org/10.1016/j.electacta.2012.01.054
19. Homborg AM, van Westing EPM, Tinga T et al (2013) Novel time–frequency characterization of electrochemical noise data in corrosion studies using Hilbert spectra. Corros Sci 66:97–110. https://doi.org/10.1016/j.corsci.2012.09.007
20. Liu C, Revilla RI, Zhang D et al (2018) Role of Al2O3 inclusions on the localized corrosion of Q460NH weathering steel in marine environment. Corros Sci 138:96–104. https://doi.org/10.1016/j.corsci.2018.04.007
21. Feng H, Jiang Z, Li H et al (2018) Influence of nitrogen on corrosion behaviour of high nitrogen martensitic stainless steels manufactured by pressurized metallurgy. Corros Sci 144:288–300. https://doi.org/10.1016/j.corsci.2018.09.002
22. Ningshen S, Sakairi M, Suzuki K, Ukai S (2014) The corrosion resistance and passive film compositions of 12% Cr and 15% Cr oxide dispersion strengthened steels in nitric acid media. Corros Sci 78:322–334. https://doi.org/10.1016/j.corsci.2013.10.015
23. Kar A, Sain S, Rossouw D et al (2016) Facile synthesis of SnO2-PbS nanocomposites with controlled structure for applications in photocatalysis. Nanoscale 8:2727–2739. https://doi.org/10.1039/c5nr07036h
24. Gao Z, Zhang D, Jiang S et al (2018) XPS investigations on the corrosion mechanism of V(IV) conversion coatings on hot-dip galvanized steel. Corros Sci 139:163–171. https://doi.org/10.1016/j.corsci.2018.04.030
25. Silversmit G, Depla D, Poelman H et al (2004) Determination of the V2p XPS binding energies for different vanadium oxidation states (V5+ to V0+). J Electron Spectrosc Relat Phenom 135:167–175. https://doi.org/10.1016/j.elspec.2004.03.004

26. Muangtong P, Rodchanarowan A, Chaysuwan D et al (2020) The corrosion behaviour of CoCrFeNi-x (x = Cu, Al, Sn) high entropy alloy systems in chloride solution. Corros Sci 172:108740. https://doi.org/10.1016/j.corsci.2020.108740
27. Zhao Y, Zhou E, Xu D et al (2018) Laboratory investigation of microbiologically influenced corrosion of 2205 duplex stainless steel by marine Pseudomonas aeruginosa biofilm using electrochemical noise. Corros Sci 143:281–291. https://doi.org/10.1016/j.corsci.2018.08.018
28. Liu C, Bi Q, Matthews A (2001) EIS comparison on corrosion performance of PVD TiN and CrN coated mild steel in 0.5 N NaCl aqueous solution. Corros Sci 43:1953–1961. https://doi.org/10.1016/S0010-938X(00)00188-8
29. Su B, Luo L, Wang B et al (2021) Annealed microstructure dependent corrosion behavior of Ti-6Al-3Nb-2Zr-1Mo alloy. J Mater Sci Technol 62:234–248. https://doi.org/10.1016/j.jmst.2020.05.058
30. Liu J-C, Park S, Nagao S et al (2015) The role of Zn precipitates and Cl− anions in pitting corrosion of Sn–Zn solder alloys. Corros Sci 92:263–271. https://doi.org/10.1016/j.corsci.2014.12.014
31. Li J, Lin X, Guo P et al (2018) Electrochemical behaviour of laser solid formed Ti–6Al–4V alloy in a highly concentrated NaCl solution. Corros Sci 142:161–174. https://doi.org/10.1016/j.corsci.2018.07.023
32. Macdonald DD (2006) Reflections on the history of electrochemical impedance spectroscopy. Electrochim Acta 51:1376–1388. https://doi.org/10.1016/j.electacta.2005.02.107
33. Ayati NS, Khandandel S, Momeni M et al (2011) Inhibitive effect of synthesized 2-(3-pyridyl)-3,4-dihydro-4-quinazolinone as a corrosion inhibitor for mild steel in hydrochloric acid. Mater Chem Phys 126:873–879. https://doi.org/10.1016/j.matchemphys.2010.12.023
34. Deffo Ayagou MD, Mai Tran TT, Tribollet B et al (2018) Electrochemical impedance spectroscopy of iron corrosion in H2S solutions. Electrochim Acta 282:775–783. https://doi.org/10.1016/j.electacta.2018.06.052
35. Hirschorn B, Orazem ME, Tribollet B et al (2010) Determination of effective capacitance and film thickness from constant-phase-element parameters. Electrochim Acta 55:6218–6227. https://doi.org/10.1016/j.electacta.2009.10.065
36. Lukács Z (1999) Evaluation of model and dispersion parameters and their effects on the formation of constant-phase elements in equivalent circuits. J Electroanal Chem 464:68–75. https://doi.org/10.1016/S0022-0728(98)00471-9
37. Bommersbach P, Alemany-Dumont C, Millet JP, Normand B (2005) Formation and behaviour study of an environment-friendly corrosion inhibitor by electrochemical methods. Electrochim Acta 51:1076–1084. https://doi.org/10.1016/j.electacta.2005.06.001
38. Alves AC, Wenger F, Ponthiaux P et al (2017) Corrosion mechanisms in titanium oxide-based films produced by anodic treatment. Electrochim Acta 234:16–27. https://doi.org/10.1016/j.electacta.2017.03.011
39. Heakal FE-T, Fekry AM, Ghoneim AA (2008) Corrosion characterization of new tin–silver binary alloys in nitric acid solutions. Corros Sci 50:1618–1626. https://doi.org/10.1016/j.corsci.2008.02.003
40. Bolat G, Izquierdo J, Santana JJ et al (2013) Electrochemical characterization of ZrTi alloys for biomedical applications. Electrochim Acta 88:447–456. https://doi.org/10.1016/j.electacta.2012.10.026
41. Hoseinpoor M, Momeni M, Moayed MH, Davoodi A (2014) EIS assessment of critical pitting temperature of 2205 duplex stainless steel in acidified ferric chloride solution. Corros Sci 80:197–204. https://doi.org/10.1016/j.corsci.2013.11.023
42. Berthomé G, Malki B, Baroux B (2006) Pitting transients analysis of stainless steels at the open circuit potential. Corros Sci 48:2432–2441. https://doi.org/10.1016/j.corsci.2005.09.012
43. Homborg AM, Cottis R, Mol JMC (2016) An integrated approach in the time, frequency and time-frequency domain for the identification of corrosion using electrochemical noise. Electrochim Acta 222:627–640. https://doi.org/10.1016/j.electacta.2016.11.018
44. Dong ZH, Shi W, Zhang GA, Guo XP (2011) The role of inhibitors on the repassivation of pitting corrosion of carbon steel in synthetic carbonated concrete pore solution. Electrochim Acta 56:5890–5897. https://doi.org/10.1016/j.electacta.2011.04.120
45. Cottis RA, Homborg AM, Mol JMC (2016) The relationship between spectral and wavelet techniques for noise analysis. Electrochim Acta 202:277–287. https://doi.org/10.1016/j.electacta.2015.11.148
46. Tang Y, Zuo Y, Zhao H (2005) The current fluctuations and accumulated pitting damage of mild steel in NaNO2–NaCl solution. Appl Surf Sci 243:82–88. https://doi.org/10.1016/j.apsusc.2004.09.094
47. Zhang Z, Li X, Zhao Z et al (2020) In-situ monitoring of pitting corrosion of Q235 carbon steel by electrochemical noise: wavelet and recurrence quantification analysis. J Electroanal Chem 879:114776. https://doi.org/10.1016/j.jelechem.2020.114776
48. Girija S, Mudali UK, Khatak HS, Raj B (2007) The application of electrochemical noise resistance to evaluate the corrosion resistance of AISI type 304 SS in nitric acid. Corros Sci 49:4051–4068. https://doi.org/10.1016/j.corsci.2007.04.007
49. Hernández M, Genescá J, Uruchurtu J, Barba A (2009) Correlation between electrochemical impedance and noise measurements of waterborne coatings. Corros Sci 51:499–510. https://doi.org/10.1016/j.corsci.2008.12.011
50. Klapper HS, Goellner J (2009) Electrochemical noise from oxygen reduction on stainless steel surfaces. Corros Sci 51:144–150. https://doi.org/10.1016/j.corsci.2008.10.009
51. Homborg AM, Tinga T, Zhang X et al (2013) Transient analysis through Hilbert spectra of electrochemical noise signals for the identification of localized corrosion of stainless steel. Electrochim Acta 104:84–93. https://doi.org/10.1016/j.electacta.2013.04.085
52. Brossia CS, Cragnolino GA (2004) Effect of palladium on the corrosion behavior of titanium. Corros Sci 46:1693–1711. https://doi.org/10.1016/j.corsci.2003.10.003
53. Utomo WB, Donne SW (2006) Electrochemical behaviour of titanium in H2SO4–MnSO4 electrolytes. Electrochim Acta 51:3338–3345. https://doi.org/10.1016/j.electacta.2005.09.031
54. Burstein GT (2010) 2.02 - Passivity and localized corrosion*. In: Cottis B, Graham M, Lindsay R et al (eds) Shreir's corrosion. Elsevier, Oxford, pp 731–752
55. Fernández-Domene RM, Blasco-Tamarit E, García-García DM, Antón JG (2013) Passivity breakdown of titanium in LiBr solutions. J Electrochem Soc 161:C25. https://doi.org/10.1149/2.035401jes